NANO LETTERS

pubs.acs.org/NanoLett Letter

Topological Photonic Lattice for Uniform Beam Splitting, Robust Routing, and Sensitive Far-Field Steering

Tianwei Wu, Yankun Li, Xilin Feng, Shuang Wu, Zihe Gao, and Liang Feng*

Cite This: *Nano Lett.* 2023, 23, 3866−3871 Read Online

ACCESS | Metrics & More | Article Recommendations | Supporting Information

ABSTRACT: Far-field optical beam steering is a fast-growing technology for communications, spatial ranging, and detections. Nonmechanical optical phased arrays based on straight waveguides have been studied recently, where the beam emission angle to the propagation axis can be scanned by conveniently tuning the wavelength. However, the dispersion of the waveguide limits the wavelength sensitivity of beam steering and the deliberately created emitters inevitably introduce in-line backscattering on-chip. To overcome these limitations, here, we report a robust and back-reflection-free topological photonic integrated circuit, where different functionalities, such as beam splitting, routing, and far-field steering, are defined by strategic arrangements of lattices with different topological modulations simply controlled by a single lattice deformation parameter. Benefiting from the robust topological scheme, an extra band flattening is applied to achieve far-field steering with high wavelength sensitivity.

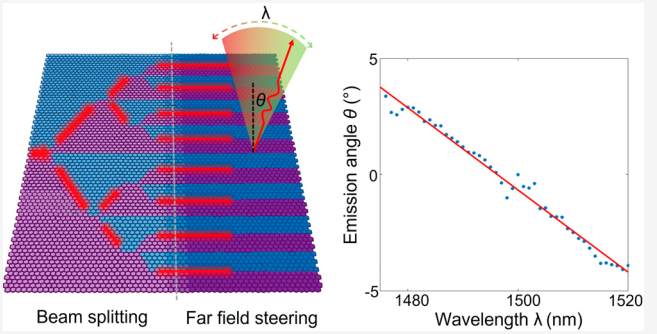

KEYWORDS: *topological photonics, chiral photonic crystal, optical routing, optical phased array*

Beam splitting and routing are fundamental features to photonic circuits. Toward a better on-chip light routing scheme, topological photonics[1−3] has garnered increasing interest in recent years. Inspired by the quantum spin Hall effect, spin-momentum locking has been demonstrated in various photonic platforms[4−8] where the polarization of light locks with the direction of the momentum. Similarly, because the left-handed or right-handed circular polarizations of the in-plane electric field can be treated as pseudospins,[9−11] topological photonic crystals can support a unidirectional propagation for each spin at the domain interfaces over a large range of frequency defined by the bulk bandgap. Such propagation remains intact even at abrupt turns and sharp corners, offering an elegant solution to the backscattering-free beam routing for on-chip guided light. Therefore, these robust topologically protected gapless chiral modes are suitable to build versatile and broadband topological photonic integrated circuits. Although most applications of topological photonics have been focused on topological lasers[12,13] and resonators,[14,15] the successful demonstration of topological light routing[16] has exhibited the feasibility of applying topological states of light to create a fully connected integrated photonic network. Here we further expand the potential of topological photonics by achieving broadband uniform beam splitting and sensitive far-field steering for another state-of-the-art mainstream technology in photonics, namely, optical phased arrays (OPA).

Compared with its predecessor, radio frequency phased array antenna,[17] OPA[18−23] is currently in rapid development due to a higher working frequency and a broader bandwidth intrinsically associated with the optical domain. To date, most of the OPAs are based on parallel waveguide arrays,[24−26] where the far-field emission from the emitters is determined jointly by the inter-waveguide phase differences (angle φ along the phased-array axis) and the waveguide dispersion (angle θ along the wavelength-controlled axis; for example, see Figure 1). The manipulation of θ is limited by the dispersion of a straight waveguide. As a consequence, only limited scanning sensitivity such as 0.15°/nm with vertical emissions is possible, at a working wavelength in the telecom band around 1500 nm.[24] To reach a higher scanning sensitivity, on the other hand, several practices involving photonic crystals have been made. For example, slow-light photonic crystal defect waveguides are investigated to build phased arrays,[27,28] where the group index and mode dispersion can be engineered to a greater extent. However, both the emitters in the parallel waveguide array and the imperfect fabrication of the topologically trivial photonic crystal induce back-reflection. Unless complicated interference between multiplayer structures can be constructed,[29] the quality of the emitted beam inevitably deteriorates.

Received: February 6, 2023
Revised: April 20, 2023
Published: April 24, 2023

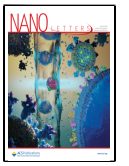

https://doi.org/10.1021/acs.nanolett.3c00474
Nano Lett. 2023, 23, 3866−3871

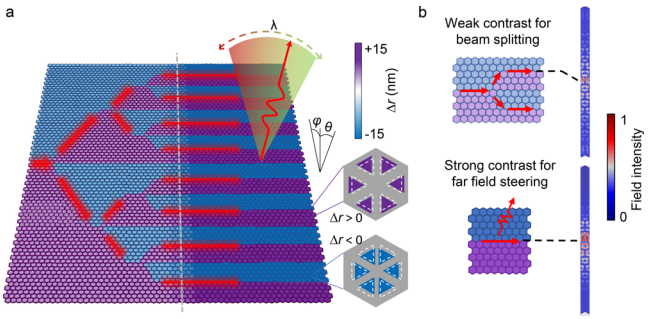

Figure 1. Topological photonic lattices with beam splitting, routing, and far-field steering. (a) Schematic of the hybrid-domain photonic crystal device. The color represents the displacement of the holes in each hexagonal unit cell. The unit cells of the shrunk ($\Delta r < 0$) and expanded ($\Delta r > 0$) lattice are shown in the right two insets. Here, incident light along the central interface from the left is uniformly split into eight parallel channels by the cascaded splitters enabled by the topological lattices with a weaker displacement contrast. In this region, light is guided at the interface between adjacent topologically trivial ($\Delta r < 0$) and nontrivial ($\Delta r > 0$) domains (light blue and purple). The right part of the circuit consists of topological lattices with a stronger displacement contrast, where guided light at the topological interface between two adjacent domains (deep blue ($\Delta r < 0$) and purple ($\Delta r > 0$)) can efficiently couple to the free space. Here, the topological interface is designed to favor a specific emitting angle θ as a function of operation wavelengths. (b) Configuration of a 1-to-2 splitting unit and a single emitting interface and their corresponding near-field mode profiles near the interface marked by the black dashed lines.

Accordingly, our attempt is to explore far-field beam steering in the topological photonic crystal while tapping into its topologically protected light routing in the near-field. Here, we demonstrate a topological photonic circuit with strategic arrangements of topological and trivial hybrid domains. By tuning a single lattice deformation parameter Δr, we tailor the near-field mode profiles as guided light travels through different stages of our circuit to enable uniform 1-to-8 beam splitting, robust routing, and subsequent far-field beam scanning with a wavelength sensitivity up to 0.31°/nm around 1500 nm.

The topologically protected light propagation in our device (denoted by red arrows in Figure 1a) originates from the strategic arrangement of topological and trivial domains of photonic crystals. Here, the topological modulation is enabled by deforming the honeycomb lattice. Each hexagonal unit cell of the topological photonic crystal consists of six equilateral triangular holes, which are shifted either inward or outward to the center by a small distance Δr to form a shrunken (blue, $\Delta r < 0$) or expanded (purple, $\Delta r > 0$) lattice without changing the size of the unit cell. Although both positive and negative Δr support an optical bandgap for TE modes, a band inversion near the Γ point in the k-space only occurs in the expanded lattice when $\Delta r > 0$: the lower frequency bands near the Γ point are *d*-orbit-like quadrupole modes, and the higher bands are *p*-orbit-like dipole modes in the expanded lattice, corresponding to a topologically nontrivial bandgap with a $\mathbb{Z}_2$ index of 1.[9,10,30] Contrarily, the bandgap in the shrunken lattice is topologically trivial with a $\mathbb{Z}_2$ index of 0. Because the bandgap must be closed at the interface of the topologically trivial and nontrivial lattice domains, as a consequence, a gapless interface state supporting unidirectional and chiral light propagation emerges. This interface state is robust and immune to defects and disorders, by virtue of the topological protection. It is also this topological protection that makes the topological photonic crystal an ideal integrated platform for a large variety of on-chip photonic information applications including, but not limited to, waveguiding, routing, networking, and signal processing.[14,15,31] Compared to other topological photonic platforms, the topological photonic crystal with the shrunk-and-expanded modulation exhibits excellent robustness due to its intrinsic large bulk bandgap and simultaneously favors the vertical emission for the far-field beam steering.

To implement a large-scale circuit with versatile functions, our device contains multiple regions with different Δr contrasts distinguished by both the sign and the magnitude of the displacement parameter Δr. Specifically, our topological photonic circuit illustrated in Figure 1a consists of a routing region and an emitting region. By deliberate design of Δr, we tune the topological modulation strength and hence the functions that each region can realize.

The routing region on the left has three layers of cascaded splitters for 1-to-8 beam splitting. To achieve a broadband uniform splitting, the topological domains in this region are designed for a weak contrast modulation. This is quantified by $\Delta r = \pm 7.5$ nm with the same magnitude but opposite signs on the two sides of the interface, shown in the top left of Figure 1b. Because of the weak contrast, the topological interface mode becomes less confined in the transverse direction for more uniform modal overlap with two output branches of the splitter. This can also be verified from the near-field mode profile simulation of an interface in top right of Figure 1b where the topological mode expands into multiple hexagonal unit cells, featuring a more uniform power splitting.

The emitting region consists of parallel topological interfaces for coherent far-field emission and beam steering (bottom left of Figure 1b), which has a flatter dispersion than a straight waveguide and is also free from backscattering due to the topological protection. Different from the intentionally introduced scatters in parallel waveguide arrays, surface emission naturally takes place along the vertical direction in our device as the chiral state exists in the proximity of the Γ point in the k-space (thus above the light line). Here, a strong contrast displacement $\Delta r = \pm 15$ nm facilitates stronger surface emission, which is desired for far-field beam steering.

Cascading the routing and emitting regions entails a spectral overlap of the bandgaps where two topological interface modes in two regions reside. Hence, we study the optical band structures of the topological photonic crystals and the dispersion of the interface modes with different Δr contrasts. The dispersions associated with interfaces with a weak contrast of $\Delta r = \pm 7.5$ nm and a strong contrast of $\Delta r = \pm 15$ nm are plotted in Figures 2a and 2b, respectively. A bandgap opens between two bulk bands (black dots) in both cases, within which two counterpropagating gapless topological interface modes with opposite pseudospins (denoted by red and gray) appear. The band structures with different Δr contrasts are spectrally aligned, making it possible to combine multiple domains in one setting: Despite a slight frequency shift, the bulk bandgaps shows a significant overlap (between two green dashed lines) of approximately 6 THz, which defines the working bandwidth of our multiregion topological circuit. The large bandgap also indicates the robustness of the topological system, such that random perturbation in fabrication cannot deteriorate the in-gap topological states. The width of the bandgap and the working bandwidth of our device can be

https://doi.org/10.1021/acs.nanolett.3c00474
Nano Lett. 2023, 23, 3866−3871

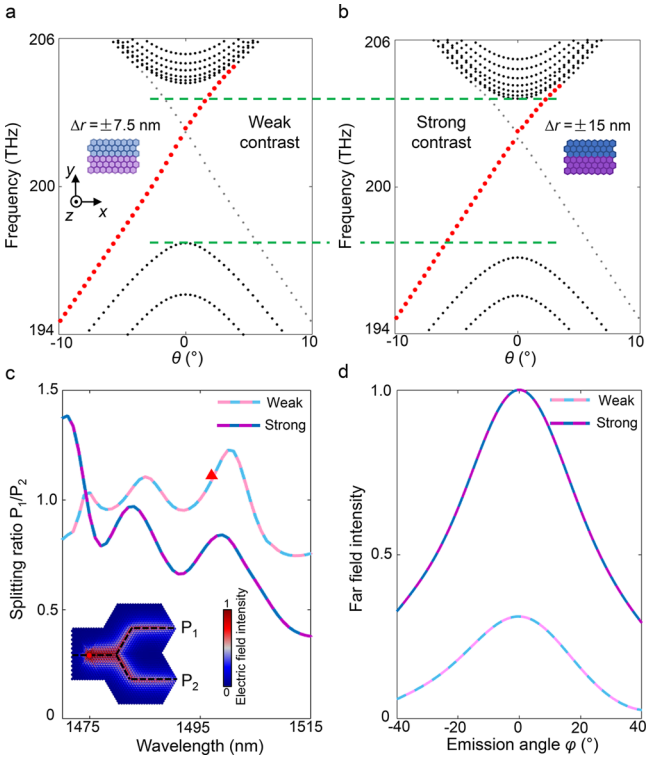

Figure 2. Topological interface modes with different displacement contrast. (a, b) Full-wave simulations of the one-dimensional band structure of the topological interface with a weak displacement contrast (Δr = ±7.5 nm) and a strong displacement contrast (Δr = ±15 nm). The wavevector is converted to the emission angle by $\theta = \arcsin(k_x/k_0)$. The top and bottom black dots denote bulk modes, and the gapless modes marked with red and gray are topological interface modes of two different spins. The red ones with positive group index are excited in the experiments. The frequency overlap between bulk bandgaps (marked by green dashed lines) is the working bandwidth of the device with hybrid domains. (c) Power splitting ratio between two output paths in a splitting unit. The inset shows the electric field distribution at the wavelength marked by the red triangle. (d) Far-field emission intensity from a single super unit cell of the topological interface mode at $\theta = 0$. The emission angle φ is the polar angle in the yz-plane.

further increased if using air cladding (see the Supporting Information, Section 1).

Note that although an abrupt change of the Δr contrast occurs across two regions, the back-reflection is forbidden because the spin−orbit locking mechanism remains the same across the entire topological circuit. Protected by the intrinsic topology, the forward propagating light retains its direction regardless of the change in Δr due to the lack of back-propagation channels under the same pseudospin (see the Supporting Information, Section 2).

In Figure 2c,d, we further demonstrate how the Δr contrast is tailored in each region to preferentially enhance its corresponding function. Weak Δr contrast facilitates a more uniform beam splitting in the routing region: full-wave simulations of the 1-to-2 splitting unit in Figure 2c show a good overall uniformity for the photonic crystal with the weak contrast (Δr = ±7.5 nm), where the power splitting ratio (P_1/P_2) between two output branches is within a range of 1 ± 0.25 in the whole working bandwidth (see the Supporting Information, Section 3). Strong Δr contrast produces a stronger emission in the emitting region. When Δr = 0, the lattice is reduced to an unperturbed honeycomb (graphene) lattice, and the working wavelength corresponds to the nonradiative modes below the light cone. A nonzero Δr creates supercells and band folding, which in turn create coupling to the free space and enable vertical emission (see the Supporting Information, Section 4). Therefore, the far-field emission intensity increases with the Δr contrast. The vertical emission intensity from the topological interface with strong contrast is 3 times greater compared to the one with the weak contrast according to the full-wave simulations, as shown in Figure 2d.

Our topological integrated circuit was fabricated on the silicon-on-insulator (SOI) platform. Figure 3a shows its optical microscopy image and details in a unit cell revealed by the scanning electron microscopy (SEM) image. A transition region (area between the red and green dashed lines) with an intermediate Δr contrast (Δr = ±10 nm and Δr = ±12.5 nm) is designed to further enhance the coupling efficiency between two regimes.

Experimentally, a tunable continuous-wave (CW) laser is used to excite the topological interface mode. The incident light is linearly polarized and focused on the single topological interface near the left boundary of the device (Figure 3b). To image the device, a cross-polarization polarizer is used to filter out the incident light. The focused laser covers a range of incident angles, enabling the excitation of the interface states with different wavelengths. At the point of incidence, both pseudospins, which correspond to modes with left-handed or right-handed circularly polarized in-plane electric field, can be excited simultaneously under the linearly polarized excitation. The unidirectional and chiral topological interface dictates that modes with two different spins propagate in opposite directions along the interface. Only the right-propagating interface mode can couple into the device while the one propagating to the left is diffracted into the unpatterned silicon slab. Inside the device the light is then split into eight branches after three stages of cascaded splitters in the splitting region. Comparing the emission intensity in the propagation direction x along the eight parallel topological interface emitters in Figure 3b, we experimentally observed that the intensity becomes stronger after the green dashed line, which demonstrates the emission enhancement after transition into the strong-contrast region. Note that imperfect fabrication may lead to less confinement of the topological modes at the interface, but the topological nature of the photonic crystal remains. Despite slight penetration of light into the bulk in some areas, the interface mode remains to be topologically protected and thus maintains all the desired properties. In this scenario, the modes are still well guided without backscattering along the topological interfaces. As the distance between two adjacent excited parallel interfaces is around 20 μm (32 hexagonal units), the coupling between them is negligible even with the increased penetration caused by imperfect fabrication, which ensures a linear dispersion of the topological interface mode for the far-field beam steering by tuning the operation wavelength. To clearly quantify the enhancement of emitting strength, the integrated optical power in the transverse direction over eight parallel interfaces is shown in Figure 3c, where the highest emission intensity occurs upon the light's entering into the emitting region. The far-field patterns (Figure 3d) are captured with an iris at the image plane (see the Supporting Information, Section 6), selecting only the emission from the parallel interfaces (the emitters). By tuning

https://doi.org/10.1021/acs.nanolett.3c00474
Nano Lett. 2023, 23, 3866−3871

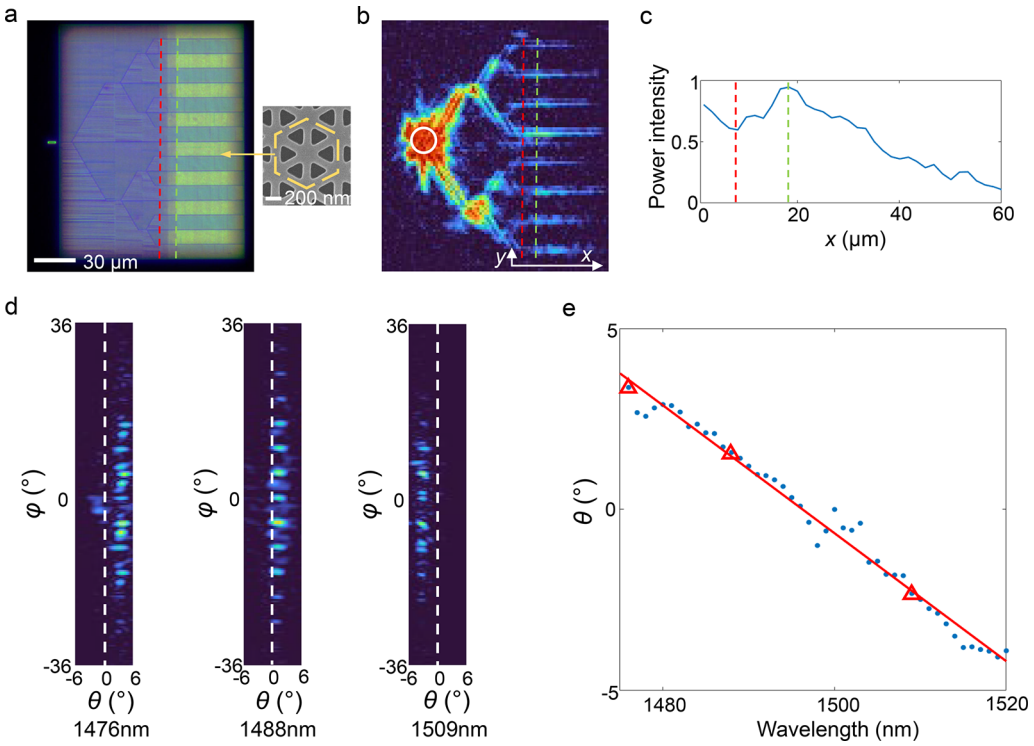

Figure 3. Characterization of the topological hybrid-domain integrated photonic circuit. (a) Dark-field optical microscopy image of the device (left) and the scanning electron microscopy (SEM) image of one hexagonal unit cell (right). (b) Image of the device under optical excitation (marked by the white circle). (c) Total optical power measured along the propagation direction, integrating over the transverse direction along y. (d) Far-field emission pattern from the strong-contrast emitter region with different incident wavelengths. (e) Steering of the emission angle (θ) versus excitation wavelength. Blue dots are the measured data, and the red line is a linear regression. The red triangles mark the emission wavelengths shown in (d).

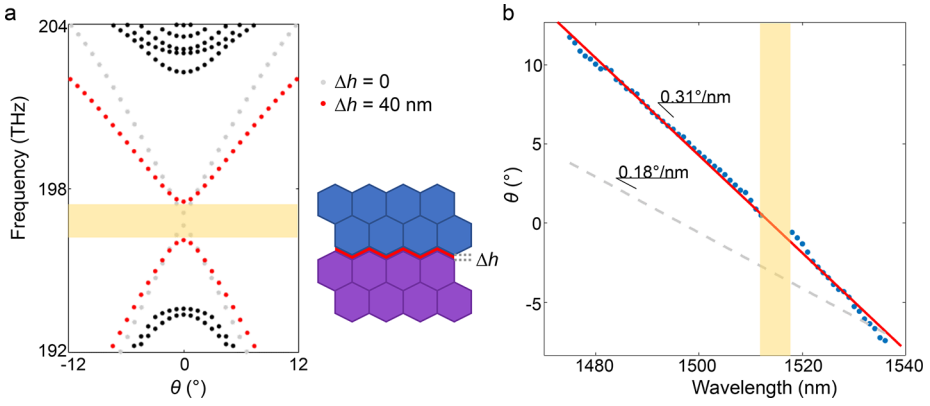

Figure 4. Band flattening for higher steering wavelength sensitivities. (a) Simulated band structure of the photonic crystal with (red) and without (gray) a spatial domain gap (red zigzag shape region shown in the right bottom inset). The yellow region marks the small bandgap of the interface mode. (b) Measured steering of the emission angle. The yellow region marks the bandgap shown by the experimental data. The gray dashed line represents the linear fitting of the measured data from the previous device without a domain gap in Figure 3e.

the wavelength, a directional far-field emission can be achieved according to the dispersion of the topological interface modes. In total, a 7.8° steering angle (Figure 3e) is observed during a 44 nm wavelength scan, showing a θ-angle tuning sensitivity of 0.18°/nm.

To further improve the wavelength sensitivity of the steering angle, we now study the phase-matching condition (i.e., $k_0 \sin\theta = k$, where k_0 and k are the wave vectors in the free space and guided mode and θ is the emission angle). The angle tuning sensitivity strongly depends on the dispersion (i.e., $d\omega/dk$) of the propagation mode:

$$\frac{d\theta}{d\lambda_0} = -\frac{c}{\lambda_0 \cos\theta}\left(\frac{1}{d\omega/dk} - \frac{\sin\theta}{c}\right) \quad (1)$$

where c is the speed of light and λ_0 denotes the free space wavelength. According to eq 1, to realize a higher angle tuning sensitivity around the vertical direction, we need a flatter mode dispersion. Here we engineered the dispersion of the interface mode by introducing an unetched spatial gap[32] between the topological and trivial domains (Figure 4a, bottom right). Compared to the topological modes in the lattice without the domain gap (gray dots), the interface modes with a gap of Δh

https://doi.org/10.1021/acs.nanolett.3c00474
Nano Lett. 2023, 23, 3866−3871

= 40 nm (red dots) have a flatter dispersion and thus a higher wavelength sensitivity for far-field steering. This is also confirmed by the scanning measurements (Figure 4b) on our device with spatial domain gaps (see the Supporting Information, Section 8). Despite a small bandgap (marked in yellow), an overall scanning sensitivity of 0.31°/nm is achieved, which is a 2× improvement over a straight waveguides array working around the vertical direction.

By implementing a dual-contrast scheme, in conclusion, we simultaneously manipulated the near-field guided mode confinement and far-field emission intensity of the topological photonic crystal. We realized a topological photonic circuit with uniform optical beam splitting, robust routing, and sensitive far-field steering, all braided by a single lattice deformation parameter Δr. Our topological photonic platform holds great promise for feasible and flexible directional far-field emission and optical broadband signal processing at large.

■ ASSOCIATED CONTENT

Supporting Information

The Supporting Information is available free of charge at https://pubs.acs.org/doi/10.1021/acs.nanolett.3c00474.

Numerical simulations, including band structures with different claddings, the performance of splitting, routing, and far-field emission; fabrication procedures; illustration of the optical measurement setup; measurement of the beam divergence; additional figures for far-field emission (PDF)

■ AUTHOR INFORMATION

Corresponding Author

Liang Feng − *Department of Materials Science and Engineering and Department of Electrical and Systems Engineering, University of Pennsylvania, Philadelphia, Pennsylvania 19104, United States*; Email: fenglia@seas.upenn.edu

Authors

Tianwei Wu − *Department of Materials Science and Engineering, University of Pennsylvania, Philadelphia, Pennsylvania 19104, United States*; orcid.org/0000-0002-1960-1864

Yankun Li − *Department of Electrical and Systems Engineering, University of Pennsylvania, Philadelphia, Pennsylvania 19104, United States*

Xilin Feng − *Department of Electrical and Systems Engineering, University of Pennsylvania, Philadelphia, Pennsylvania 19104, United States*

Shuang Wu − *Department of Materials Science and Engineering, University of Pennsylvania, Philadelphia, Pennsylvania 19104, United States*

Zihe Gao − *Department of Materials Science and Engineering, University of Pennsylvania, Philadelphia, Pennsylvania 19104, United States*; orcid.org/0000-0003-1844-0541

Complete contact information is available at: https://pubs.acs.org/10.1021/acs.nanolett.3c00474

Author Contributions

T.W. and L.F. conceived the idea. T.W. and X.F. performed the simulations. X.F. fabricated the samples. Y.L. and T.W. performed measurements. L.F. supervised the project. All authors contributed to discussions and manuscript preparation.

Funding

We acknowledge the support from the Army Research Office (ARO) (W911NF-21-1-0148) and the National Science Foundation (NSF) (ECCS-1846766). This work was partially supported by NSF through the University of Pennsylvania Materials Research Science and Engineering Center (MRSEC) (DMR-1720530) and performed in part at the Singh Center for Nanotechnology, which is supported by the NSF National Nanotechnology Coordinated Infrastructure Program under Grant NNCI-1542153.

Notes

The authors declare no competing financial interest.

■ REFERENCES

(1) Lu, L.; Joannopoulos, J. D.; Soljačić, M. Topological Photonics. *Nat. Photonics* **2014**, *8* (11), 821−829.

(2) Ozawa, T.; Price, H. M.; Amo, A.; Goldman, N.; Hafezi, M.; Lu, L.; Rechtsman, M. C.; Schuster, D.; Simon, J.; Zilberberg, O.; Carusotto, I. Topological Photonics. *Rev. Mod. Phys.* **2019**, *91* (1), 015006.

(3) Khanikaev, A. B.; Mousavi, S. H.; Tse, W.-K.; Kargarian, M.; MacDonald, A. H.; Shvets, G. Photonic Topological Insulators. *Nat. Mater.* **2013**, *12* (3), 233−239.

(4) Barik, S.; Karasahin, A.; Flower, C.; Cai, T.; Miyake, H.; DeGottardi, W.; Hafezi, M.; Waks, E. A Topological Quantum Optics Interface. *Science* **2018**, *359* (6376), 666−668.

(5) Dong, J.-W.; Chen, X.-D.; Zhu, H.; Wang, Y.; Zhang, X. Valley Photonic Crystals for Control of Spin and Topology. *Nat. Mater.* **2017**, *16* (3), 298−302.

(6) Shalaev, M. I.; Walasik, W.; Tsukernik, A.; Xu, Y.; Litchinitser, N. M. Robust Topologically Protected Transport in Photonic Crystals at Telecommunication Wavelengths. *Nat. Nanotechnol.* **2019**, *14* (1), 31−34.

(7) Liu, W.; Hwang, M.; Ji, Z.; Wang, Y.; Modi, G.; Agarwal, R. Z2 Photonic Topological Insulators in the Visible Wavelength Range for Robust Nanoscale Photonics. *Nano Lett.* **2020**, *20* (2), 1329−1335.

(8) Liu, W.; Ji, Z.; Wang, Y.; Modi, G.; Hwang, M.; Zheng, B.; Sorger, V. J.; Pan, A.; Agarwal, R. Generation of Helical Topological Exciton-Polaritons. *Science* **2020**, *370* (6516), 600−604.

(9) Wu, L.-H.; Hu, X. Scheme for Achieving a Topological Photonic Crystal by Using Dielectric Material. *Phys. Rev. Lett.* **2015**, *114* (22), 223901.

(10) Barik, S.; Miyake, H.; DeGottardi, W.; Waks, E.; Hafezi, M. Two-Dimensionally Confined Topological Edge States in Photonic Crystals. *New J. Phys.* **2016**, *18* (11), 113013.

(11) Gao, F.; Xue, H.; Yang, Z.; Lai, K.; Yu, Y.; Lin, X.; Chong, Y.; Shvets, G.; Zhang, B. Topologically Protected Refraction of Robust Kink States in Valley Photonic Crystals. *Nat. Phys.* **2018**, *14* (2), 140−144.

(12) Bahari, B.; Ndao, A.; Vallini, F.; El Amili, A.; Fainman, Y.; Kanté, B. Nonreciprocal Lasing in Topological Cavities of Arbitrary Geometries. *Science* **2017**, *358* (6363), 636−640.

(13) Bahari, B.; Hsu, L.; Pan, S. H.; Preece, D.; Ndao, A.; El Amili, A.; Fainman, Y.; Kanté, B. Photonic Quantum Hall Effect and Multiplexed Light Sources of Large Orbital Angular Momenta. *Nat. Phys.* **2021**, *17* (6), 700−703.

(14) Ma, J.; Xi, X.; Sun, X. Topological Photonic Integrated Circuits Based on Valley Kink States. *Laser Photonics Rev.* **2019**, *13* (12), 1900087.

(15) Barik, S.; Karasahin, A.; Mittal, S.; Waks, E.; Hafezi, M. Chiral Quantum Optics Using a Topological Resonator. *Phys. Rev. B Condens. Matter* **2020**, *101* (20), 205303.

(16) Zhao, H.; Qiao, X.; Wu, T.; Midya, B.; Longhi, S.; Feng, L. Non-Hermitian Topological Light Steering. *Science* **2019**, *365* (6458), 1163−1166.

(17) Visser, H. J. *Array and Phased Array Antenna Basics*; John Wiley & Sons: Chichester, 2005.

(18) Hsu, C.-P.; Li, B.; Solano-Rivas, B.; Gohil, A. R.; Chan, P. H.; Moore, A. D.; Donzella, V. A Review and Perspective on Optical Phased Array for Automotive LiDAR. *IEEE J. Sel. Top. Quantum Electron.* **2021**, *27* (1), 1−16.
(19) He, J.; Dong, T.; Xu, Y. Review of Photonic Integrated Optical Phased Arrays for Space Optical Communication. *IEEE Access* **2020**, *8*, 188284−188298.
(20) McManamon, P. F.; Dorschner, T. A.; Corkum, D. L.; Friedman, L. J.; Hobbs, D. S.; Holz, M.; Liberman, S.; Nguyen, H. Q.; Resler, D. P.; Sharp, R. C.; Watson, E. A. Optical Phased Array Technology. *Proc. IEEE* **1996**, *84* (2), 268−298.
(21) Kim, I.; Martins, R. J.; Jang, J.; Badloe, T.; Khadir, S.; Jung, H.-Y.; Kim, H.; Kim, J.; Genevet, P.; Rho, J. Nanophotonics for Light Detection and Ranging Technology. *Nat. Nanotechnol.* **2021**, *16* (5), 508−524.
(22) Sun, J.; Timurdogan, E.; Yaacobi, A.; Hosseini, E. S.; Watts, M. R. Large-Scale Nanophotonic Phased Array. *Nature* **2013**, *493* (7431), 195−199.
(23) Dostart, N.; Zhang, B.; Khilo, A.; Brand, M.; Al Qubaisi, K.; Onural, D.; Feldkhun, D.; Wagner, K. H.; Popović, M. A. Serpentine Optical Phased Arrays for Scalable Integrated Photonic Lidar Beam Steering. *Optica* **2020**, *7* (6), 726.
(24) Kwong, D.; Hosseini, A.; Covey, J.; Zhang, Y.; Xu, X.; Subbaraman, H.; Chen, R. T. On-Chip Silicon Optical Phased Array for Two-Dimensional Beam Steering. *Opt. Lett.* **2014**, *39* (4), 941−944.
(25) Hutchison, D. N.; Sun, J.; Doylend, J. K.; Kumar, R.; Heck, J.; Kim, W.; Phare, C. T.; Feshali, A.; Rong, H. High-Resolution Aliasing-Free Optical Beam Steering. *Optica* **2016**, *3* (8), 887.
(26) Miller, S. A.; Chang, Y.-C.; Phare, C. T.; Shin, M. C.; Zadka, M.; Roberts, S. P.; Stern, B.; Ji, X.; Mohanty, A.; Jimenez Gordillo, O. A.; Dave, U. D.; Lipson, M. Large-Scale Optical Phased Array Using a Low-Power Multi-Pass Silicon Photonic Platform. *Optica* **2020**, *7* (1), 3.
(27) Vercruysse, D.; Sapra, N. V.; Yang, K. Y.; Vučković, J. Inverse-Designed Photonic Crystal Circuits for Optical Beam Steering. *ACS Photonics* **2021**, *8* (10), 3085−3093.
(28) Kondo, K.; Tatebe, T.; Hachuda, S.; Abe, H.; Koyama, F.; Baba, T. Fan-Beam Steering Device Using a Photonic Crystal Slow-Light Waveguide with Surface Diffraction Grating. *Opt. Lett.* **2017**, *42* (23), 4990−4993.
(29) Michaels, A.; Yablonovitch, E. Inverse Design of near Unity Efficiency Perfectly Vertical Grating Couplers. *Opt. Express* **2018**, *26* (4), 4766−4779.
(30) Parappurath, N.; Alpeggiani, F.; Kuipers, L.; Verhagen, E. Direct Observation of Topological Edge States in Silicon Photonic Crystals: Spin, Dispersion, and Chiral Routing. *Sci. Adv.* **2020**, *6* (10), No. eaaw4137.
(31) Chen, Y.; He, X.-T.; Cheng, Y.-J.; Qiu, H.-Y.; Feng, L.-T.; Zhang, M.; Dai, D.-X.; Guo, G.-C.; Dong, J.-W.; Ren, X.-F. Topologically Protected Valley-Dependent Quantum Photonic Circuits. *Phys. Rev. Lett.* **2021**, *126* (23), 230503.
(32) Wen, E.; Bisharat, D. J.; Davis, R. J.; Yang, X.; Sievenpiper, D. F. Designing Topological Defect Lines Protected by Gauge-Dependent Symmetry Indicators. *Phys. Rev. Applied* **2022**, *17* (6), 064008.

https://doi.org/10.1021/acs.nanolett.3c00474
Nano Lett. 2023, 23, 3866−3871